Real- time interaction analysis of Shiga toxins and membrane microdomains of primary human brain microvascular endothelial cells

Keywords: detergent-resistant membranes / glycosphingolipids / lipid rafts / pHBMECs / surface acoustic wave

Johanna Detzner[2], Daniel Steil[2], Gottfried Pohlentz[2], Nadine Legros[2], Hans-Ulrich Humpf[3], Alexander Mellmann[2], Helge Karch[2], and Johannes Müthing[1,2]

[2]Institute for Hygiene, University of Münster, D-48149 Münster, Germany

[3]Institute for Food Chemistry, University of Münster, D-48149 Münster, Germany

Running title: Interaction of Stxs with microdomains of pHBMECs

[1]Corresponding author:

Prof. Dr. Johannes Müthing

Institute for Hygiene

University of Münster

Robert-Koch-Str. 41

D-48149 Münster

Germany

e-mail: jm@uni-muenster.de, phone: +49.251.83 55192, fax: +49.251.83 55341

Supplementary data is available:

Figure S1. Detection of Stx receptors Gb3Cer and Gb4Cer and the *lipid raft* marker cholesterol in sucrose density gradient fractions of pHBMECs (replicate 2).

Figure S2. MS^1 spectra of Gb3Cer (**A**), Gb4Cer (**B**), and PLs (**C**) obtained from DRM fraction F2 of pHBMECs (replicate 2).

Figure S3. MS^2 spectrum of Gb3Cer (d18:1, C24:1/C24:0) (**A**) and corresponding fragmentation scheme (**B**) obtained from DRM fraction F2 of pHBMECs (replicate 2).

Figure S4. MS^2 spectrum of Gb4Cer (d18:1, C24:1/C24:0) (**A**) and corresponding fragmentation scheme (**B**) obtained from DRM fraction F2 of pHBMECs (replicate 2).

Figure S5. MS^1 spectra of Gb3Cer (**A**), Gb4Cer (**B**), and PLs (**C**) obtained from nonDRM fraction F7 of pHBMECs (replicate 2).

Figure S6. SAW real-time interaction sensorgrams obtained for binding of Stx2a towards DRM (**A**) and nonDRM fractions (**B**) prepared from pHBMECs (replicate 2).

Figure S7. SAW real-time interaction sensorgrams obtained for binding of Stx2e towards DRM fractions prepared from pHBMECs (replicate 1).

Table SI. Absolute and relative cholesterol amounts in the sucrose gradient fractions of the two replicates of pHBMECs.

Table SII. Calculated association k_{ass} and dissociation k_{diss} rate constants and equilibrium dissociation constant K_D for Stx2a and Stx2e using DRMs derived from pHBMECs.

Abstract

Infections of the human intestinal tract with enterohemorrhagic *Escherichia coli* (EHEC) result in massive extraintestinal complications due to translocation of EHEC-released Shiga toxins (Stxs) from the gut into the circulation. Stx-mediated damage of the cerebral microvasculature raises serious brain dysfunction being the most frequent cause of acute mortality in patients suffering from severe EHEC infections. Stx2a and Stx2e are associated with heavy and mild course of infection, respectively. Stx2a preferentially binds to globotriaosylceramide (Gb3Cer, Galα1-4Galβ1-4Glcβ1-1Cer), while Stx2e prefers globotetraosylceramide (Gb4Cer, GalNAcβ1-3Galα1-4Galβ1-4Glcβ1-1Cer). Both glycosphingolipids (GSLs) were detected in detergent-resistant membranes (DRMs) of primary human brain microvascular endothelial cells (pHBMECs) resembling microdomains of the plasma membrane. In this study we show that Gb3Cer and Gb4Cer of pHBMECs with saturated C16:0, C22:0, and C24:0 fatty acids dominated in DRMs, corresponding to the liquid-ordered membrane phase, whereas lipoforms carrying unsaturated C24:1 and C24:2 fatty acids prevailed in the nonDRM fractions, which correspond to the liquid-disordered membrane phase. Similarly, a shift of the phospholipids from saturated lipoforms in the DRM to unsaturated species in the nonDRM fractions was observed. Real-time biomolecular interaction analysis using affinity-purified Stx2a and Stx2e, recorded with a surface acoustic wave (SAW) biosensor, evidenced high binding strength of both toxins towards DRMs and failure in interaction with nonDRMs. These results support the hypothesis of preferential binding of Stxs towards microdomains harbouring GSL receptors carrying saturated fatty acids in their lipid anchors. Collectively, unravelling the precise mechanisms of Stx-microdomain interaction may help to develop antiadhesive compounds to combat Stx-mediated cellular injury.

Introduction

Shiga toxins (Stxs) belong to the group of bacterial AB_5 toxins with certain carbohydrate-binding specificities being released by Stx-producing *Escherichia coli* (STEC) (Bergan et al. 2012). Enterohemorrhagic *E. coli* (EHEC) comprise the human-pathogenic subgroup of STEC, which cause severe diarrhea and hemorrhagic colitis after ingestion and colonization of the intestinal mucosa (Schüller 2011). Upon transfer into the circulation, Stxs elicit extraintestinal complications such as the hemolytic-uremic syndrome (HUS) (Zoja et al. 2010). Moreover, Stxs activate innate immune responses that may lead to inflammation thereby increasing the severity of organ injury in patients infected with EHEC (Lee and Tesh 2019). This is further aggravated by the fact that Stx interacts with the complement system resulting in an impaired control and thus to enhanced complement activation (Orth-Höller and Würzner 2014). Interestingly, Stx-mediated toxicity towards erythroblasts during the course of erythropoiesis might contribute to the anemia caused by Stx-producing pathogens (Betz et al. 2016). In the blood neutrophilic granulocytes are generally considered “piggy-back” transporters of Stx through the circulation (te Loo et al. 2000; Brigotti et al. 2013). Damage of kidney microvascular endothelial cells underlies the pathological changes in HUS (Bielaszewska and Karch 2005; Karch et al. 2005) and injury of brain microvascular endothelial cells disturbs the blood-brain barrier function resulting in serious cerebral dysfunction (Richards and Kavanagh 2009; Obata 2010). Thus, acute renal failure can indirectly induce impairment in brain function. Neurological injury can be sudden and severe and is the most frequent cause of acute mortality in patients suffering from severe EHEC infections indicating a central role of Stx in cerebral dysfunction in this disease (Karpman et al. 2010; Trachtman et al. 2012). After attachment of the non-covalently linked

homopentameric B subunit assembly to the plasma membrane, the Stx-receptor complex is endocytosed, transported via a retrograde pathway to the endoplasmic reticulum and translocated to the cytosol, where the catalytic A1 portion exert its ribotoxic effect (Sandvig et al. 2010; Bergan et al. 2012; Johannes 2017).

Among the various Stx subtypes, Stx2a (in previous and recent publications often inaccurately termed Stx2; for revised nomenclature of Stx-subtypes refer to Scheutz et al. 2012) represents the most important subtype being more frequently associated with HUS than other Stx subtypes (Davis et al. 2014; Melton-Celsa 2014; Kampmeier et al. 2018), while presence of Stx2e may predict a milder disease with minimal risk of HUS (Friedrich et al. 2002). All Stxs analysed until now bind to glycosphingolipids (GSLs) of the globo-series (Raa et al. 2009; Lingwood et al. 2010), which are characteristic cell surface-exposed structures of the human microvascular endothelium in the kidneys and the brain (Bauwens et al. 2013; Legros et al. 2018). Certain Stx subtypes can be distinguished by their receptor binding preferences depending on the variability of the oligosaccharide chain length of Stx-binding GSLs (Müthing et al. 2012; Steil et al. 2018). Stx2a binds with high preference to globotriaosylceramide (Gb3Cer, Galα1-4Galβ1-4Glcβ1-1Cer) when compared to globotetraosylceramide (Gb4Cer, GalNAcβ1-3Galα1-4Galβ1-4Glcβ1-1Cer), while Stx2e exhibits preferred adherence towards Gb4Cer besides binding to Gb3Cer (DeGrandis et al. 1989; Keusch et al. 1995; Müthing et al. 2012).

The large structural heterogeneity of GSLs results from differences in number, identity, linkage, and anomeric configuration of the carbohydrate moieties, and also from structural differences within the hydrophobic portion (Levery 2005; Merrill 2011; D'Angelo et al. 2013; Zhang et al. 2019). GSLs are primarily located in the outer leaflet of the two-layered cell membrane, where they reside in close proximity with the phospholipid (PL) sphingomyelin (SM) and cholesterol in microdomains termed

as *lipid rafts* (Gupta and Surolia 2010; Sonnino and Prinetti 2010). Besides their inherent involvement in many cellular events (Jennemann and Gröne 2013; Russo et al. 2016), their exofacial localization in *lipid rafts* renders GSLs excellent candidates as adhesion platforms for carbohydrate-binding microorganisms and microbial toxins (Smith et al. 2004; Lencer and Saslowsky 2005; Cho et al. 2012; Aigal et al. 2015). With the aid of non-ionic detergents, segregated microdomains can be isolated from sucrose density gradients after ultracentrifugation as supramolecular clustered structures denoted as detergent-resistant membranes (DRMs) (Brown 2006). DRMs are considered equivalents for the liquid-ordered phase of cell membranes, and nonDRM fractions correspond to the liquid-disordered phase being useful tools in membrane research (London and Brown 2000; Lingwood and Simons, 2007).

Here we report on the structural differences of Gb3Cer and Gb4Cer lipoforms detectable in DRM and nonDRM fractions of pHBMECs. Furthermore, DRM and nonDRM preparations were applied to recently developed real-time interaction analysis based on surface acoustic wave (SAW) technology (Steil et al. 2018). Stxs were found to bind with high preference to DRMs in contrast to nonDRMs of pHBMECs and the achieved binding kinetics allowed for determining their binding strengths towards DRMs harbouring Stx receptor GSLs.

Results

Previous studies of us on the presence and fine structures of Stx receptors have revealed Gb3Cer and Gb4Cer as the characteristic GSLs of pHBMECs. The twin-tailed ceramide of both globo-series GSLs exhibited considerable heterogeneity due to linkage of a fatty acid with variable chain length (C16 to C24) to the uniform long-chain aminoalcohol sphingosine (d18:1). The “18:1” signifies the C18 alkyl chain length harbouring a double bond between C4 and C5, and the “d” stands for “dihydroxy”, i.e. one hydroxyl group at C1 and one at C3, whereby the one at C1 links the proximal glucose of the growing oligosaccharide at its reducing end to form the GSL core. Cer (d18:1, C16:0), Cer (d18:1, C22:0) and Cer (d18:1, C24:1/C24:0) were identified as the prevalent lipid anchors of Gb3Cer and Gb4Cer isolated from pHBMECs (Legros et al. 2017a; Legros et al. 2018). The aim of this study was to determine the occurrence of hypothesized DRM- and nonDRM-specific Gb3Cer and Gb4Cer species and the postulated preferred interaction of the subtypes Stx2a and Stx2e with DRMs versus nonDRMs of pHBMECs, which resemble the liquid-ordered and liquid-disordered membrane phase, respectively.

Distribution of Gb3Cer and Gb4Cer to DRM and nonDRM fractions

The occurrence and relative content of Gb3Cer and Gb4Cer in the sucrose gradient fractions obtained by ultracentrifugation were determined for the two biological replicates of pHBMECs employed in this study. The distribution attained for replicate 1 is shown in Figure 1 portraying the immunochemically detected relative content of Gb3Cer and Gb4Cer in Figure 1A and Figure 1B, respectively, and the relative content of the *lipid raft marker* cholesterol in Figure 1C. Gb3Cer was found to amount to 71% in added DRM fractions F1-F3 of replicate 1 suggesting association with *lipid*

rafts (Figure 1A). The same holds true for Gb4Cer exhibiting identical distribution in summed DRM fractions F1-F3 (Figure 1B). Cholesterol, determined with manganese chloride stain, served as the classical microdomain marker, which accumulated to 70% in the DRMs (Figure 1C). For comparison purposes the distribution patterns of Gb3Cer, Gb4Cer, and cholesterol of replicate 2 are provided in the Supplementary data, Figure S1 showing similar results. The absolute and relative cholesterol amounts determined in the sucrose gradient fractions of the two replicates of pHBMECs are listed in the Supplementary data, Table SI.

Molecular species of Gb3Cer, Gb4Cer, and PLs in DRMs

The ESI MS^1 spectrum of canonical DRM fraction F2 derived from pHBMECs of replicate 1 demonstrates, after removal of alkali-labile lipids, the Gb3Cer species with Cer (d18:1, C16:0), Cer (d18:1, C22:0), and Cer (d18:1, C24:1/C24:0) as the main GSLs in this fraction (Figure 2A). This distribution indicates prevalence of Gb3Cer variants each carrying a saturated fatty acid with the restriction that the Gb3Cer lipoform with C24:0 fatty acid is accompanied by less abundant C24:1 species. The proof of the proposed structures is exemplarily shown for Gb3Cer (d18:1, C24:1/C24:0) by the MS^2 spectrum in the Supplementary data, Figure S3. The MS^1 analysis gave similar results for Gb4Cer of DRM fraction F2 of pHBMECs exhibiting the same relative ion signal intensities when compared to Gb3Cer with dominance of ceramides harbouring mostly the saturated fatty acids C16:0, C22:0 and C24:0, accompanied by less abundant C24:1, in the respective Gb4Cer species (Figure 2B). An example of a proof of structure of the proposed GSL lipoforms is given for Gb4Cer (d18:1, C24:1/C24:0) with the MS^2 spectrum in the Supplementary data, Figure S4. The PL compositional analysis of DRM fraction F2 revealed most prominent signals for ions at *m/z* 760.58 and 782.57, corresponding to

monounsaturated protonated $[M+ H]^+$ and monosodiated $[M+Na]^+$ ions of PC (34:1), respectively (Figure 2C). The second most abundant PL species were the pairs of PC (32:1/32:0) in its protonated and sodiated form indicated by ions at *m/z* 732.55/734.56 and 754.53/756.54, respectively. The presence of PC (36:2/36:1) was verified by detection of $[M+Na]^+$ ions at *m/z* 808.58/810.60, whereby the monounsaturated 36:1 dominated over the diunsaturated 36:2 PC species. Ions at *m/z* 703.57 and 835.66/837.67, highlighted in grey, correspond to monosodiated SM (d18:1, C16:0) and SM (d18:1, C24:1/C24:0), respectively, indicating the presence of this *lipid raft* marker in the DRM fraction F2 of pHBMECs. Similar spectra were achieved for Gb3Cer, Gb4Cer, and the PLs in case of DRM fraction F2 derived from pHBMECs of replicate 2 as shown in the Supplementary data, Figure S2.

Molecular species of Gb3Cer, Gb4Cer, and PLs in nonDRMs

The ESI MS^1 spectra of Gb3Cer, Gb4Cer, and PLs, which were obtained from gradient fraction F7 derived from replicate 1 of HBMECs, are shown in Figure 3. Fraction F7 represents a typical nonDRM fraction containing low quantities of immunochemically detectable Gb3Cer and Gb4Cer (refer to Figure 1A and Figure 1B, respectively), associated with sizeable amounts of cholesterol (refer to Figure 1C). Detected Gb3Cer variants were those with Cer (d18:1, C24:2/C24:1) as the main and only Gb3Cer lipoforms, accompanied by a series of polyethylene glycol oligomers derived from the detergent used for solubilization (Figure 3A). Characteristic for this fraction is the occurrence of the Gb3Cer species with doubly unsaturated C24:2 fatty acid, accompanied with the slightly stronger C24:1 fatty acid carrying lipoform. The proof of proposed Gb3Cer (d18:1, C24:2/C24:1) is portrayed by the MS^2 spectrum in Figure 4. Importantly, the Gb3Cer (d18:1, C24:2) variant seems to specifically emerge in nonDRMs. In addition, the Gb3Cer lipoforms,

carrying saturated C16:0, C22:0 and C24:0 fatty acid, being usually detectable in total GSLs and DRM preparations of pHBMECs, are totally absent in the nonDRM fraction. The same holds true for Gb4Cer detected in nonDRM fraction F7 as shown in Figure 3B. More precisely, the Gb4Cer variant with doubly unsaturated C24:2 fatty acid occurs in nonDRM fraction F7, accompanied by the somewhat stronger variant with C24:1 fatty acid, both representing the only Gb4Cer species in nonDRM fraction F7. The proof of proposed Gb4Cer (d18:1, C24:2/C24:1) is demonstrated with the MS^2 spectrum in Figure 5. Furthermore, the lack of Gb4Cer lipoforms with saturated C16:0, C22:0, and C24:0 is an additional striking feature of the nonDRM fraction. The MS analysis of PLs gave presence of lyso-PC, highlighted by greyed boxes in the spectrum, and at the same time complete lack of SM ions in the nonDRM fraction F7 (Figure 3C). Most intensive monosodiated $[M+Na]^+$ ions at *m/z* 544.34, accompanied by strong $[M+H]^+$ ions with *m/z* at 522.35, could be assigned to lyso-PC (18:1). This dominant lyso-PC was accompanied by less intensive lyso-PC (16:1/16:0) ions with characteristic *m/z* values at 494.32/496.33 and 522.35/544.34, corresponding to the protonated and the sodiated species, respectively. Thus, the two lyso-PC variants could be identified as definite nonDRM markers, which were solely present in the liquid disordered but not in the liquid ordered phase of cell membranes of pHBMECs. A further difference noticed for the nonDRM fraction F7, when compared to F2, was the absence of saturated PL species and the relative increase of mono to double unsaturated PC species, for instance the rise of double unsaturated PC (34:2) at *m/z* 758.57/780.55 (protonated/sodiated) over PC (34:1) at *m/z* 760.59/782.56 (protonated/sodiated) (Figure 3C). An additional distinctive feature of the nonDRM fraction F7 was newly occurring triply unsaturated PC (36:3) at *m/z* 784.58 and 806.57 in its protonated and monosodiated form, respectively. The MS analysis of nonDRM fraction F7 derived from replicate 2 of pHBMECs yielded comparable

spectra for Gb3Cer, Gb4Cer, and the PLs as shown in the Supplementary data, Figure S5, whereby the ion signals of lyso-PC and the PC species appeared with somewhat lower intensity when compared to those of nonDRM fraction F7 obtained from replicate 1 of pHBMECs (see Figure 3C).

Real-time interaction analysis of Stx2a with DRMs and nonDRMs derived from pHBMECs

Association and dissociation curves were achieved for Stx2a by means of biomolecular interaction analysis in real time using affinity-purified Stx2a and an SAW biosensor as recently published (Steil et al. 2018). The biosensor surfaces were coated with DRMs or nonDRMs derived from replicate 1 of pHBMECs forming stable membrane layers on the biosensor surface, respectively. Increasing concentrations of Stx2a, ranging from 20 nM up to 250 nM, were applied. The association and dissociation curves achieved from this experimental set up are shown in Figure 6. The rounded individual values of the calculated association rate constant k_{ass}, the dissociation rate constant k_{diss} and the equilibrium dissociation constant K_D together with their mean values obtained from the SAW real-time interaction analysis of Stx2a with DRMs (Figure 6A) are listed in Table I. The calculated K_D mean value, which describes the average strength of binding between Stx2a and DRMs being calculated from the binding kinetics using 20, 50, 80, 120, 180 and 250 nM toxin concentrations, was 77±15 nM, indicating high affinity binding of Stx2a towards the DRM preparation. On the other hand, Stx2a exhibited no adhesion at all towards nonDRMs as shown in Figure 6B. Thus, failure of association and dissociation made any calculations superfluous. The real-time interaction analysis of Stx2a with DRMs and nonDRMs derived from replicate 2 of pHBMECs gave similar results (Supplementary data, Figure S6 and Table SII). The mean value of K_D amounted to 119±8 nM indicated a

somewhat lower binding strength of Stx2a towards DRMs in this experiment using a membrane preparation from replicate 2 of pHBMECs. However, the detected affinity ranged in the same order of magnitude when compared to replicate 1 and Stx2a failed again in binding towards nonDRMs (see Figure 6).

Real-time interaction analysis of Stx2e with DRMs and nonDRMs derived from pHBMECs

The same experimental approach was performed for studying the real-time binding of affinity-purified Stx2e towards DRM and nonDRM preparations from pHBMECs as shown in Figure 7. Due to very limited quantity of membrane material from the primary cells, the analysis of both the DRMs and the nonDRMs was only possible for replicate 2 of pHBMECs. A list of the rounded individual values of the calculated association rate constant k_{ass}, the dissociation rate constant k_{diss} and the equilibrium dissociation constant K_D together with their mean values obtained from the biomolecular interaction analysis of Stx2e with DRMs (Figure 7A) are listed in Table I. Based on the binding kinetics, the calculated K_D mean value was 165±22 nM, indicating slightly lower binding intensity of Stx2e towards DRMs when compared to Stx2a (see Figure 6A). The application of Stx2e revealed a slight but recognizable interaction of Stx2e with nonDRMs as visible in Figure 7B. However, the weakness of binding strength did neither allow for creating association and dissociation curves nor for calculation of related association and dissociation rate constants. The real-time interaction analysis of Stx2e with DRMs derived from replicate 1 of pHBMECs gave similar results (Supplementary data, Figure S7 and Table SII). The mean value of K_D amounted to 159±10 nM being almost identical with the one obtained by measurements of replicate 2 (see Figure 7 and Table I).

As a résumé it can be concluded from our SAW binding kinetics that the Stx2a and Stx2e subtypes both exhibited a strong binding strength towards DRMs and did not bind (Stx2a) or did bind very weakly (Stx2e) to nonDRMs simulating the liquid-ordered and liquid-disordered membrane phase, respectively, of pHBMECs. Although ranging in the same magnitude, Stx2a showed sizeable higher extent of adhesion capacity towards DRMs, which harbored the highest relative content of Gb3Cer and Gb4Cer content among the density gradient fractions.

Discussion

Stx causes massive damage of human brain microvascular endothelial cells and raises serious dysfunction of the central nervous system (Richards and Kavanagh 2009). Patients with cerebral involvement have a greater chance of getting severe sequelae and mortality than with HUS alone and autopsy of brains of patients suggests the weakening of the blood-brain barrier during the disease (Obata 2010). Importantly, some patients develop neurological symptoms before the onset of HUS showing direct involvement and a central role of Stx in brain dysfunction in this disease (Obata 2010). Thus, impairment of the central nervous system represents often a life-threatening condition resulting in serious long-term effects even after recovery from HUS (Spinale et al. 2013; Chan and Ng 2016). Importantly, a retrospective analysis of pediatric patients with cerebral complications during EHEC-HUS, who received early treatment with eculizumab, a monoclonal antibody that blocks the complement with favorable outcome of the disease (Würzner et al. 2014), was associated with complete regression of both kidney injury and neurological lesions (Giordano et al. 2019). The radical breakdown of the blood-brain barrier caused by Stx2e has been previously shown by us using porcine brain capillary endothelial cells as a cell culture model (Meisen et al. 2013). Owing to the high impact of Stx-mediated endothelial impairment of the cerebral vascular bed, we and other research groups have investigated in the past human brain-derived endothelial cell lines (Fujii et al. 2008; Betz et al. 2011) and primary endothelial cells of human brain (Eisenhauer et al. 2001; Stricklett et al. 2002; Ergonul et al. 2003; Legros et al. 2017a) including detection, identification and structural characterization of the GSL receptors of various Stx subtypes beside other pathophysiological aspects of this toxin. Primary cells are advantageous in terms of their resemblance to the original

tissue characteristics thus mimicking the *in vivo* phenotype more faithfully than immortalized cells or cloned cell lines (reviewed in Legros et al. 2018). However, albeit having the Stx-binding GSL receptors identified the initial attachment process of Stx to membrane-inserted GSL receptors remains yet poorly understood.

Previous findings revealed the presence of different lipoforms of Gb3Cer and Gb4Cer in total GSLs from pHBMECs harbouring GSL species with ceramides overwhelmingly composed of sphingosine (d18:1) as the invariable portion of the lipid anchor and variable fatty acids videlicet C16:0, C22:0 or C24:1/C24:0 as the main Stx receptors (Legros et al. 2017a; Legros et al. 2018). In the recent investigations a shifting from saturated lipoforms of glycerophospholipids in the DRM to unsaturated species in the nonDRM fractions was observed, using the F2 and F7 fractions as representative fractions of the liquid-ordered and liquid-disordered membrane phase, respectively (Legros et al. 2017a). Here, we now scrutinized (in addition to the glycerophospholipids) the fine structures of the Gb3Cer and Gb4Cer species, which occurred in DRM and nonDRM fractions. Lipoforms with onefold unsaturated C24:1 fatty acid were found being specifically enriched in DRM fraction F2, while lipoforms with twofold unsaturated C24:2 fatty acid were exclusively detected in the F7 fraction. Noteworthy, the Gb3Cer and Gb4Cer variants each with doubly unsaturated C24:2 fatty acid have never been before identified in total GSLs and DRM fractions of human brain endothelial cells or human endothelial cells from other vascular beds. Co-localization of Gb3Cer and Gb4Cer species containing a saturated fatty acid with PC molecules carrying mostly saturated fatty acids together with the canonical *lipid raft* markers SM and cholesterol supports the hypothesis of supposed *lipid raft* similarity of DRMs representing the liquid-ordered membrane phase. Analogously, the predominance of Gb3Cer and Gb4Cer lipoforms with one- and diunsaturated fatty acid accompanied with PC species carrying mostly unsaturated fatty acids and lyso-

PC underlines the resemblance of the nonDRMs with the liquid-disordered membrane phase corresponding to *non-lipid raft* membrane organization. Although the reason for the structural differences regarding degree of unsaturation remains elusive, one can speculate that Gb3Cer, Gb4Cer and PC lipoforms in vicinity with SM and planar cholesterol molecules might stabilize the *raft* assembly in plasma membranes. Summing the constraint, investigations on DRMs, which represent an effective tool to approach the dynamics of Stx interaction with GSL-containing lipid microdomains (Nutikka and Lingwood 2004), allow for principal suggestions of conceivable arrangement of Stx-binding GSLs in membranous microdomain clusters of human endothelial cells (Legros et al. 2018).

Presentation of the glycan parts of GSLs in the exofacial leaflet of the plasma membrane protruding into the environment predestines GSLs as attachment sites of a number of pathogens such as bacteria and pathogen-derived virulence factors (Karlsson 1989; Smith et al. 2004). In addition to specific affinity to a certain glycan, the lipid moiety contributes to an efficient binding and uptake of a carbohydrate-binding toxin or bacterial adhesin suggesting a functional role of *lipid rafts* to gain entry into cells (Sandvig et al. 2014; Aigal et al. 2015; Zuverink and Barbieri 2018). SM and cholesterol residing in close proximity with GSLs are further key membrane constituents of *lipid rafts* (Gupta and Surolia 2010; Sonnino and Prinetti 2010; García-Arribas et al. 2016) being involved in forming membrane domains, promoting separation of membranes into liquid-ordered and liquid-disordered phases and lateral sorting by cholesterol-mediated hydrophobic matching (Kaiser et al. 2011; Abe and Kobayashi 2014). Importantly, association with plasma membrane microdomains has been shown in previous studies to be a pivotal requirement for efficient binding and internalization of Stxs (Lingwood et al. 2010; Sandvig et al. 2014) and, furthermore, the occurrence of Stx-receptor Gb3Cer in *lipid rafts* is deemed to play a central role in

the pathology of HUS (Khan et al. 2009). Fatty acid-mediated fluidity within Gb3Cer/cholesterol DRM vesicle constructs has been shown to selectively regulate GSL carbohydrate binding (Mahfoud et al. 2009) and association of Stx with DRMs is an essential requirement in the endoplasmic reticulum for a cytotoxic effect (Smith et al. 2006). It is therefore tempting to speculate that certain Gb3Cer lipoforms of pHBMECs found in this study to co-distribute with cholesterol and SM in DRMs may be of functional impact in efficient binding and internalization of Stx. Gb3Cer and Gb4Cer species with Cer (d18:1, C16:0), Cer (d18:1, C22:0) and Cer (d18:1, C24:0), the prevalent GSL lipoforms with saturated fatty acid occurring in DRMs, accompanied by Cer (d18:1, C24:1) lipoforms with onefold unsaturated fatty acid, are the candidates. Their dominance in DRMs, the liquid-ordered membrane phase, seems to predestine preferred interaction with Stx, whereas prevalence of Gb3Cer and Gb4Cer with Cer (d18:1, C24:2) carrying a twofold unsaturated fatty acid in nonDRMs, the liquid-disordered membrane phase, along with reduced amounts of the saturated Gb3Cer and Gb4Cer species, would indicate a less pronounced role in binding, internalization and retrograde transportation of the toxin.

Exploring the precise mechanisms underlying the initial attachment of Stx to the membrane surface is a matter of intensive research. To establish this approach we previously used model membranes spiked with Gb3Cer reference of human source, which were applied for coating the chip surface with a lipid bilayer (Steil et al. 2018). Real-time interaction analysis revealed strong binding preference of Stx2a and Stx2e to DRMs of pHBMECs, whereby Stx2e exhibited weak adhesion and Stx2a no binding at all towards nonDRMs. Recorded SAW binding kinetics allowed for determining the differing binding strengths of Stx2a and Stx2e towards *lipid raft*-associated Stx receptors in the DRM preparations. Roughly calculated approximate average values of the two biological replicates (see Table I and Supplementary data,

Table SII) each revealed an equilibrium dissociation constant K_D for Stx2a of 98 nM and for Stx2e an K_D value of 162 nM indicating somewhat less intensive binding of Stx2e (the higher the K_D, the lower the binding strength). This indicates a rather slight difference when compared to significant differences of K_D measurements of 124 nM for Stx2a and 1481 nM for Stx2e when applying fabricated model membranes loaded with Gb3Cer only (Steil et al. 2018). Since DRMs of pHBMECs contain Gb4Cer in addition to Gb3Cer and because Gb4Cer is known as the favorite receptor of Stx2e (DeGrandis et al. 1989; Müthing et al. 2012), the weak binding to Gb3Cer in model membranes (Steil et al. 2018) seems to be compensated by additional Gb4Cer in pHBMEC-derived DRMs as shown in this study. This explains the similar binding strength of Stx2a and Stx2e when using DRMs of pHBMECs.

Previous real-time kinetic analysis of binding between Stx and Gb3Cer by Nakajima and co-workers using surface plasmon resonance (SPR) revealed K_D values of 222 nM for Stx1 and 1044 nM for Stx2 (Nakajima et al. 2001). Interestingly, although employing differing experimental settings, data were comparable to our previous results reflecting the same order of magnitude of K_D calculations (Steil et al. 2018). Another SPR approach was reported by Soltyk and colleagues, where the authors describe (among others) the interaction of an Stx1-derived pentameric B-subunit with a model membrane (Soltyk et al. 2002). These SPR measurements gave a K_D value of 3 nM for $Stx1B_5$ being much lower than those previously reported for SPR measurements using Stx holotoxins (Nakajima et al. 2001). Similarly, low nanomolar K_D values were obtained for StxB interacting with two hydroxylated Gb3-C24:1 diastereoisomers, employing SPR interaction analysis (Schütte et al. 2015). The authors adapted the experimental procedure of Nakajima and collaborators (Nakajima et al. 2001) and achieved K_D values in the single- to double-digit nanomolar range (Schütte et al. 2015). Of note, Gb3-decorated human serum

albumin interacted with surface-immobilized Stx1 and Stx2 reaching K_D values of 39 and 101 nM, respectively, determined by real-time SPR analysis (Maria Cherian et al. 2014). Collectively, from this data we can conclude that many parameters such as the molecular environment of Stx receptors within the lipid layer in general and, more precisely, the structural differences of individual lipid constituents and the glycan presentation as well as the concentration and purity of the Stx subtypes may exacerbate the interpretation of the discussed real-time interaction analyses.

Conclusions

To the best of our knowledge, our study is the first report on direct application of membrane preparations derived from human brain endothelium simulating the liquid-ordered and liquid-disordered membrane phase, respectively, to real-time interaction analysis. In addition, real-time interaction analysis of Stxs and target cell membranes gives a further proof of the applicability of the SAW technology (Hoß and Bendas 2017) and opens up promising perspectives to investigations on newly produced Stx glycoconjugates aimed at inhibition of and protection against Stxs (Sharon 2006; Kavaliauskiene et al. 2017) such as pectin-derived neoglycolipids (Pohlentz et al. 2019). We hope that our study will contribute to the development of novel strategies in the fight against infectious diseases.

Materials and methods

Propagation of pHBMECs

Primary human brain microvascular endothelial cells (pHBMECs) were purchased from ScienCell™ (Carlsbad, CA, USA; cat. no. 1000). The lowercase “p” stands for “primary” to distinguish this and some other studies of our group (Legros et al. 2017a; Legros et al. 2018) from previous works where immortalized endothelial cells or endothelial cell lines have been used (Bauwens et al. 2011; Betz et al. 2011). The primary cells were maintained and passaged following established procedures (Legros et al. 2017a; Legros et al. 2018). pHBMECs were propagated in 175 cm^2 tissue culture flasks (Greiner Bio-One, Frickenhausen, Germany) in endothelial cell medium without antibiotics not exceeding passage 7.

Preparation of sucrose density gradient fractions from pHBMECs

Sucrose density gradient fractions were prepared following the original description of Brown and Rose (Brown and Rose 1992) with minor modifications as previously described (Betz et al. 2011; Steil et al. 2015; Legros et al. 2018). Briefly, confluent grown pHBMECs were homogenized in lysis buffer and remnant cell debris was removed by mild centrifugation (400 x *g*). Membranes were then separated from cytosol by short ultracentrifugation (150,000 x *g*) of the supernatant. The membrane sediment was dissolved in 1% Triton X-100 buffer and mixed with the same portion of 85% sucrose. The resulting 42.5% sucrose solution was then overlayed with a discontinuous gradient of 30% and 5% sucrose. Eight fractions of 1.5 mL each were collected stepwise from the top of the gradient after ultracentrifugation (200,000 x *g*): three upper DRM-associated fractions (F1 to F3) and five lower nonDRM fractions (F4 to F8) (Legros et al. 2018).

Isolation of GSLs, cholesterol, and PLs from gradient fractions

The 1.5 mL aliquots obtained from the sucrose gradient fractions were dialyzed against deionized water, freeze-dried and resolved in chloroform/methanol (2/1, v/v) corresponding to 5 x 10^5 cells/µL. A volume of 100 µL of each of the eight fractions, equivalent to 5 x 10^7 cells, was withdrawn and utilized for TLC and MS analysis of GSLs and TLC detection of cholesterol. For this purpose, glycerophospholipids and triacylglycerols were removed by saponification using 1 N methanolic NaOH following previously published protocols (Kouzel et al. 2013; Legros et al. 2017a; Legros et al. 2017b). A volume of 20 µL of fraction F2 and F7, corresponding to 1 x 10^7 cells, was removed and employed for MS analysis of PLs. Combined fractions F1 to F3 and fraction F7 (remaining material) were dried, weighted and adjusted to a concentration of 1 mg/mL in PBS supplemented with 5 mM $MgCl_2$ to be used for the preparation of small unilamellar vesicles (SUVs) required for ensuing biomolecular interaction analysis measurements (see below).

TLC detection of cholesterol and GSLs

Aliquots of alkaline-treated sucrose gradient fractions were applied onto silica gel 60 precoated glass plates (HPTLC plates, size 10 cm x 10 cm, thickness 0.2 mm, no. 1.05633.0001; Merck, Darmstadt, Germany) with an automatic sample applicator (Linomat 5, CAMAG, Muttenz, Switzerland). Cholesterol was separated in chloroform/aceton (96/4, v/v) and GSLs were chromatographed in chloroform/methanol/water (120/70/17, each by vol). Cholesterol was stained with manganese(II) chloride (Goswami and Frey 1970; Kouzel et al. 2013; Steil et al. 2015; Legros et al. 2017b) and the globo-series GSLs Gb3Cer and Gb4Cer were

detected using the TLC overlay assay as previously described (Kouzel et al. 2013; Steil et al. 2015). Briefly, after TLC separation the silica gel layer was fixed with 0.5% (w/v) polyisobutylmethacrylate (Plexigum P28, Röhm, Darmstadt, Germany) solution and the Stx receptor GSLs were immunostained with primary chicken anti-Gb3Cer and anti-Gb4Cer antibodies in conjunction with secondary alkaline phosphatase (AP)-conjugated anti-chicken IgY antibody (both at 1:2000 dilution). Rabbit anti-chicken IgY (code 303-055-033) secondary antibody was from Dianova (Hamburg, Germany). Detection was performed with 0.05% (w/v) 5-bromo-4-chloro-3-indolyl phosphate *p*-toluidine salt (BCIP) generating an AP-mediated blue precipitate. Manganese(II) chloride-stained cholesterol and TLC immunodetected GSL bands were densitometrically quantified with a CD 60 scanner (Desage, Heidelberg, Germany, software ProQuant®, version 1.06.000) using the reflectance mode. Pink-brownish cholesterol and dark blue immunopositive GSL bands were quantitatively measured at wavelengths of λ = 365 nm and λ = 630 nm, respectively (Kouzel et al. 2013; Steil et al. 2015; Legros et al. 2017b). A preparation of neutral GSLs from human erythrocytes, harbouring Gb3Cer and Gb4Cer, served as reference and positive control for the TLC overlay assays (Meisen et al. 2005). The nomenclature of the GSLs follows the IUPAC-IUB recommendations 1997 (Chester 1998). Reference cholesterol (cat. no. C8667) was from Sigma-Aldrich (Steinheim, Germany).

Production of affinity-purified Stx2a and Stx2e

Stx2a (in previous publications referred to as Stx2, now changed to Stx2a following the recommendations of Scheutz et al. (2012) for correct nomenclature) and Stx2e were purified from the Stx2a-producing EHEC wild-type strain of serotype O111:H- (strain 03-06016) (Zhang et al. 2007) and the Stx2e-releasing STEC wild-type strain of serotype ONT:H- (strain 2771/97) (Muniesa et al. 2000), respectively, both from

the collection of the Institute for Hygiene of the University of Münster (Münster, Germany) as recently described in detail (Steil et al. 2018). In short, the Stx-producing *E. coli* strains were cultured in growth medium supplemented with 0.5 µg/mL mitomycin C (Sigma-Aldrich), and sterile filtrated Stx-containing supernatants were produced as previously described (Müthing et al. 2012). The ensuing affinity-purification follows a recently published instruction (Steil et al. 2018). Briefly, Stx-containing supernatants were reduced to a volume of 1 mL and incubated with Gb3-derivatized magnetic beads. Upon elution and desalting, the purified toxins were finally suspended in PBS with 5 mM $MgCl_2$ and stored at -20°C until use. Purity of the Stx2a and Stx2e preparations was monitored by SDS-PAGE, the structural integrity of both toxins was checked by mass spectrometry, and their binding specificity was determined using GSL preparations from Vero cells as recently extensively described (Steil et al. 2018).

Electrospray ionization mass spectrometry (ESI MS)

GSLs of the alkaline-treated DRM F2 and the nonDRM F7 fractions derived from pHBMECs as well as the glycerophospholipids from native F2 and F7 fractions were dissolved in chloroform/methanol (1/4, v/v) and subjected to ESI MS using a SYNAPT G2-S mass spectrometer (Waters, Manchester, UK) in the positive ion sensitivity mode as explained in antecedent publications (Steil et al. 2015; Kouzel et al. 2017; Pohlentz et al. 2019). The source settings were: source temperature 80°C, capillary voltage 0.8 kV, sampling cone voltage 20 V, and offset voltage 50 V. For low energy collision-induced dissociation (CID) experiments (MS^2), precursor ions were selected with the quadrupole analyser, subjected to ion mobility separation with the following settings: wave velocity 800 - 1200 m/s, wave height 40 V, nitrogen gas flow rate 90 mL/min, and helium gas flow rate 180 mL/min. MS^1 ions were fragmented in

the transfer cell using a collision gas (Ar) flow rate of 2.0 mL/min and collision energies up to 100 eV (E_{lab}). The fragment ions were assigned according to the nomenclature of Domon and Costello (Domon and Costello1988a; Domon and Costello 1988b).

Biomolecular real-time interaction analysis using surface acoustic wave

The previously developed procedure for analyzing the biomolecular interaction of Stxs with Gb3Cer-spiked model membranes (Steil et al. 2018) was employed in this study to direct measurements of Stx interaction with DRM and nonDRM fractions obtained from pHBMECs. To this end, SUVs were prepared from pooled DRM fractions F1 to F3 and the nonDRM fraction F7, respectively, according to a published protocol (Steil et al. 2018) with minor modifications. Concisely, aliquots of 1 mg of dried lipids were dissolved in 1 mL PBS with 5 mM $MgCl_2$ and incubated in a sonication water bath generating large multilamellar lipid vesicles. SUVs were prepared with a mini-extruder (Avanti Polar Lipids Inc., Alabaster, AL, USA) by extrusion of the multilamellar vesicles through a polycarbonate membrane with 100 nm pore size (Whatman® Nucleopore™ Track-Etched Membranes, GE Healthcare, Maidstone, UK) and should be stored thereafter at 4°C no longer than 24 h until use. The surface acoustic wave (SAW) instrument SAM®5 blue (SAW Instruments GmbH, Bonn, Germany) was employed for advanced real-time, label-free measurement of biomolecular interaction. The gold surface of the biosensor chips, functionalized with 11-mercaptoundecanoic acid, was used for measurements and SUVs were applied in concentrations of 1 mg/mL. Unspecifically adsorbed SUVs were removed with 10 mM aqueous NaOH followed by coating the biosensor surface with bovine serum albumin to prevent unspecific binding of the Stxs. Stx2a and Stx2e subtypes were applied with increasing concentrations of 20, 50, 80, 120, 180, and 250 nM in PBS with 5 mM

$MgCl_2$. After the dissociation phase remaining Stx was removed with 0.5 M melibiose (Galα1-6Glc; melibiose monohydrate, cat. no. 4223.3, Carl Roth GmbH+Co KG, Karlsruhe, Germany) in PBS with 5 mM $MgCl_2$. Changes in the phase shift φ were recorded online. From the calculated values of k_{obs} ("obs" denotes "observed") and the concentration c of the ligand (videlicet Stx) the association and dissociation rate constants k_{ass} and k_{diss} were mathematically defined from the slope of the linear regression function according to the equation $k_{obs} = k_{ass} \cdot c + k_{diss}$. The equilibrium dissociation constant K_D was calculated from the quotient $K_D = k_{diss} / k_{ass}$ following the currently published detailed description (Steil et al. 2018).

Supplementary data

Supplementary data for this article are available online at http://glycob.oxfordjournals.org/.

Acknowledgements

The expert technical assistance of Dagmar Mense, Nikola Skutta, and Ralph Fischer is gratefully acknowledged.

Conflict of interest statement

None declared.

Abbreviations

DRM(s), detergent-resistant membrane(s); EHEC, enterohemorrhagic *Escherichia coli*; Gb3Cer, globotriaosylceramide; Gb4Cer, globotetraosylceramide; GSL(s), glycosphingolipid(s); HUS, hemolytic-uremic syndrome; PC, phosphatidylcholine; pHBMECs, primary human brain microvascular endothelial cells; PL(s),

phospholipid(s); SM, sphingomyelin; SPR, surface plasmon resonance; STEC, Stx-producing *Escherichia coli*; Stx, Shiga toxin; SUV(s), small unilamellar vesicle(s); TLC, thin-layer chromatography;.

Funding

This work was supported by grants from the German Research Foundation (DFG), grant number MU845/7-1 with reference number 404813761 (J.M.) and project B04 of the SFB 1009 (A.M. and H.K.), and the German Federal Ministry of Education and Research (BMBF), conducted under the umbrella of the German Center for Infection Research (DZIF, TTU 06.801) with assistance of InfectControl 2020 (TFP-TV8-AS12, ref. no. 03ZZ0802H) and InfectControl 2020 IRMRESS (ref. no. 03ZZ0805B).

References

Abe M, Kobayashi T. 2014. Imaging local sphingomyelin-rich domains in the plasma membrane using specific probes and advanced microscopy. *Biochim Biophys Acta*. 1841:720-726.

Aigal S, Claudinon J, Römer W. 2015. Plasma membrane reorganization: a glycolipid gateway for microbes. *Biochim Biophys Acta*. 1853:858-871.

Bauwens A, Bielaszewska M, Kemper B, Langehanenberg P, von Bally G, Reichelt R, Mulac D, Humpf HU, Friedrich AW, Kim KS, et al. 2011. Differential cytotoxic actions of Shiga toxin 1 and Shiga toxin 2 on microvascular and macrovascular endothelial cells. *Thromb Haemost*. 105:515-528.

Bauwens A, Betz J, Meisen I, Kemper B, Karch H, Müthing J. 2013. Facing glycosphingolipid-Shiga toxin interaction: dire straits for endothelial cells of the human vasculature. *Cell Mol Life Sci*. 70:425-457.

Bergan J, Dyve Lingelem AB, Simm R, Skotland T, Sandvig K, 2012. Shiga toxins. *Toxicon*. 60:1085-1107.

Betz J, Bielaszewska M, Thies A, Humpf HU, Dreisewerd K, Karch H, Kim KS, Friedrich AW, Müthing J. 2011. Shiga toxin glycosphingolipid receptors in microvascular and macrovascular endothelial cells: differential association with membrane lipid raft microdomains. *J Lipid Res*. 52:618-634.

Betz J, Dorn I, Kouzel IU, Bauwens A, Meisen I, Kemper B, Bielaszewska M, Mormann M, Weymann L, Sibrowski W, et al. 2016. Shiga toxin of enterohaemorrhagic *Escherichia coli* directly injures developing human erythrocytes. *Cell Microbiol*. 18:1339-1348.

Bielaszewska M, Karch H. 2005. Consequences of enterohaemorrhagic *Escherichia coli* infection for the vascular endothelium. *Thromb Haemost*. 94:312-318.

Brigotti M, Carnicelli D, Arfilli V, Tamassia N, Borsetti F, Fabbri E, Tazzari PL, Ricci F, Pagliaro P, Spisni E, et al. 2013. Identification of TLR4 as the receptor that recognizes Shiga toxin in human neutrophils. *J Immunol*. 191:4748-4758.

Brown DA, Rose JK. 1992. Sorting of GPI-anchored proteins to glycolipid-enriched membrane subdomains during transport to the apical cell surface. *Cell*. 68:533-544.

Brown DA. 2006. Lipid rafts, detergent-resistant membranes, and raft targeting signals. *Physiology*. 21:430-439.

Chan YS, Ng TB. 2016. Shiga toxins: from structure and mechanism to applications. *Appl Microbiol Biotechnol*. 100:1597-1610.

Chester MA. 1998. IUPAC-IUB Joint Commission on Biochemical Nomenclature (JCBN). Nomenclature of glycolipids-recommendations 1997. *Eur J Biochem*. 257:293-298.

Cho JA, Chinnapen DJ, Aamar E, te Welscher YM, Lencer WI, Massol R. 2012. Insights on the trafficking and retro-translocation of glycosphingolipid-binding bacterial toxins. *Front Cell Infect Microbiol*. 2:51.

D'Angelo G, Capasso S, Sticco L, Russo D. 2013. Glycosphingolipids: synthesis and functions. *FEBS J*. 280:6338-6353.

Davis TK, van de Kar NC, Tarr PI. 2014. Shiga toxin/verocytotoxin-producing *Escherichia coli* infections: practical clinical perspectives. *Microbiol Spectr*. 2:EHEC-0025-2014.

DeGrandis S, Law H, Brunton J, Gyles C, Lingwood CA. 1989. Globotetraosylceramide is recognized by the pig edema disease toxin. *J Biol Chem*. 264:12520-12525.

Domon B, Costello CE. 1988a. Structure elucidation of glycosphingolipids and gangliosides using high-performance tandem mass spectrometry. *Biochemistry*. 27:1534-1543.

Domon B, Costello CE. 1988b. A systematic nomenclature for carbohydrate fragmentation in FAB-MS/MS spectra of glycoconjugates. *Glycoconj J*. 5:397-409.

Eisenhauer PB, Chaturvedi P, Fine RE, Ritchie AJ, Pober JS, Cleary TG, Newburg DS. 2001. Tumor necrosis factor alpha increases human cerebral endothelial cell Gb_3 and sensitivity to Shiga toxin. *Infect Immun*. 69:1889-1894.

Ergonul Z, Hughes AK, Kohan DE. 2003. Induction of apoptosis of human brain microvascular endothelial cells by Shiga toxin 1. *J Infect Dis*. 187:154-158.

Friedrich AW, Bielaszewska M, Zhang WL, Pulz M, Kuczius T, Ammon A, Karch H. 2002. *Escherichia coli* harboring Shiga toxin 2 gene variants: frequency and association with clinical symptoms. *J Infect Dis*. 185:74-84.

Fuji J, Wood K, Matsuda F, Carneiro-Filho BA, Schlegel KH, Yutsudo T, Binnington-Boyd B, Lingwood CA, Obata F, Kim KS, et al. 2008. Shiga toxin 2 causes apoptosis in human brain microvascular endothelial cells via C/EBP homologous protein. *Infect Immun*. 76:3679-3689.

García-Arribas AB, Alonso A, Goñi FM. 2016. Cholesterol interactions with ceramide and sphingomyelin. *Chem Phys Lipids.* 199:26-34.

Goswami SK, Frey CF. 1970. Manganous chloride spray reagent for cholesterol and bile acids on thin-layer chromatograms. *J Chromatogr.* 53:389-390.

Giordano P, Netti GS, Santangelo L, Castellano G, Carbone V, Torres DD, Martino M, Sesta M, Di Cuonzo F, Resta MC, et al. 2019. A pediatric neurologic assessment score may drive the eculizumab-based treatment of *Escherichia coli*-related hemolytic uremic syndrome with neurological involvement. *Pediatr Nephrol*. 34:517-527.

Gupta G, Surolia A. 2010. Glycosphingolipids in microdomain formation and their spatial organization. *FEBS Lett*. 584:1634-1641.

Hoß SG, Bendas G. 2017. Mass-sensitive biosensor systems to determine the membrane interaction of analytes. *Methods Mol Biol.* 1520:145-157.

Jennemann R, Gröne HJ. 2013. Cell-specific *in vivo* functions of glycosphingolipids: lessons from genetic deletions of enzymes involved in glycosphingolipid synthesis. *Prog Lipid Res*. 52:231-248.

Johannes L. 2017. Shiga toxin - a model for glycolipid-dependent and lectin-driven endocytosis. *Toxins* (Basel). 9:pii:E340.

Kaiser HJ, Orlowski A, Róg T, Nyholm TK, Chai W, Feizi T, Lingwood D, Vattulainrn I, Simons K. 2011. Lateral sorting in model membranes by cholesterol-mediated hydrophobic matching. *Proc Natl Acad Sci USA*. 108:16628-16633.

Kampmeier S, Berger M, Mellmann A, Karch H, Berger P. 2018. The 2011 German enterohemorrhagic *Escherichia coli* O104:H4 outbreak - the danger is still out there. *Curr Top Microbiol Immunol*. 416:117-148.

Karch H, Tarr PI, Bielaszewska M. 2005. Enterohaemorrhagic *Escherichia coli* in human medicine. *Int J Med Microbiol*. 295:405-418.

Karlsson KA. 1989. Animal glycosphingolipids as membrane attachment sites for bacteria. *Annu Rev Biochem*. 58:309-350.

Karpman D, Sartz L, Johnson S. 2010. Pathophysiology of typical hemolytic uremic syndrome. *Semin Thromb Hemost*. 36:575-585.

Kavaliauskiene S, Dyve Lingelem AB, Skotland T, Sandvig K. 2017. Protection against Shiga toxins. *Toxins* (Basel). 9:pii:E44.

Keusch GT, Jacewicz M, Acheson DW, Donohue-Rolfe A, Kane AV, McCluer RH. 1995. Globotriaosylceramide, Gb3, is an alternative functional receptor for Shiga-like toxin 2e. *Infect Immun*. 63:1138-1141.

Khan F, Proulx F, Lingwood CA. 2009. Detergent-resistant globotriaosyl ceramide may define verotoxin/glomeruli-restricted haemolytic uremic syndrome pathology. *Kidney Int*. 75:1209-1216.

Kouzel IU, Pohlentz G, Storck W, Radamm L, Hoffmann P, Bielaszewska M, Bauwens A, Cichon C, Schmidt AM, Mormann M, et al. 2013. Association of Shiga toxin glycosphingolipid receptors with membrane microdomains of toxin-sensitive lymphoid and myeloid cells. *J Lipid Res*. 54:692-710.

Kouzel IU, Pohlentz G, Schmitz JS, Steil D, Humpf HU, Karch H, Müthing J. 2017. Shiga toxin glycosphingolipid receptors in human Caco-2 and HCT-8 colon epithelial cell lines. *Toxins* (Basel). 9:pii:E338.

Lee MS, Tesh VL. 2019. Roles of Shiga toxins in immunopathology. *Toxins* (Basel). 11:212.

Legros N, Dusny S, Humpf HU, Pohlentz G, Karch H, Müthing J. 2017a. Shiga toxin glycosphingolipid receptors and their lipid membrane ensemble in primary human blood-brain barrier endothelial cells. *Glycobiology*. 27:99-109.

Legros N, Pohlentz G, Runde J, Dusny S, Humpf HU, Karch H, Müthing J. 2017b. Colocalization of receptors for Shiga toxins with *lipid rafts* in primary human renal glomerular endothelial cells and influence of D-PDMP on synthesis and distribution of glycosphingolipid receptors. *Glycobiology*. 27:947-965.

Legros N, Pohlentz G, Steil D, Müthing J. 2018. Shiga toxin-glycosphingolipid interaction: status quo of research with focus on primary human brain and kidney endothelial cells. *Int J Med Microbiol*. 308:1973-1084.

Lencer WI, Saslowsky D. 2005. Raft trafficking of AB_5 subunit bacterial toxins. *Biochim Biophys Acta*. 1746:314-321.

Levery SB. 2005. Glycosphingolipid structural analysis and glycosphingolipidomics. *Methods Enzymol*. 405:300-369.

Lingwood CA, Binnington B, Manis A, Branch DR. 2010. Globotriaosyl ceramide receptor function - where membrane structure and pathology intersect. *FEBS Lett*. 584:1879-1886.

Lingwood D, Simons K. 2007. Detergent resistance as a tool in membrane research. *Nat Protoc*. 2:2159-2165.

London E, Brown DA. 2000. Insolubility of lipids in Triton X-100: physical origin and relationship to sphingolipid/cholesterol membrane domains (rafts). *Biochim Biophys Acta.* 1508:182-195.

Mahfoud R, Manis A, Lingwood CA. 2009. Fatty acid-dependent globotriaosyl ceramide receptor function in detergent resistant model membranes. *J Lipid Res*. 50:1744-1755.

Maria Cherian R, Gaunitz S, Nilsson A, Liu J, Karlsson NG, Holgersson J. 2014. Shiga-like toxin binds with high avidity to multivalent O-linked blood group P1 determinants on mucin-type fusion proteins. *Glycobiology*. 24:26-38.

Meisen I, Friedrich AW, Karch H, Witting U, Peter-Katalinić J, Müthing J. 2005. Application of combined high-performance thin-layer chromatography immunostaining and nanoelectrospray ionization quadrupole time-of-flight tandem mass spectrometry to the structural characterization of high- and low-affinity binding ligands of Shiga toxin 1. *Rapid Commun Mass Spectrom*. 19:3659-3665.

Meisen I, Rosenbrück R, Galla HJ, Hüwel S, Kouzel IU, Mormann M, Karch H, Müthing J. 2013. Expression of Shiga toxin 2e glycosphingolipid receptors of primary porcine brain endothelial cells and toxin-mediated breakdown of the blood-brain barrier. *Glycobiology*. 23:745-759.

Melton-Celsa AR. 2014. Shiga toxin (Stx) classification, structure, and function. *Microbiol Spectr*. 2:EHEC-0024-2013.

Merrill AH Jr. 2011. Sphingolipid and glycosphingolipiud metabolic pathways in the era of sphingolipidomics. *Chem Rev*. 111:6387-6422.

Müthing J, Meisen I, Zhang W, Bielaszewska M, Mormann M, Bauerfeind R, Schmidt MA, Friedrich AW, Karch H. 2012. Promiscuous Shiga toxin 2e and its intimate relationship to Forssman. *Glycobiology*. 22:849-862.

Muniesa M, Recktenwald J, Bielaszewska M, Karch H, Schmidt H. 2000. Characterization of a Shiga toxin 2e-converting bacteriophage from an *Escherichia coli* strain of human origin. *Infect Immun.* 68:4850-4855.

Nakajima H, Kiyokawa N, Katagiri YU, Taguchi T, Suzuki T, Sekino T, Mimori K, Ebata T, Saito M, Nakao H, et al. 2001. Kinetic analysis of binding between Shiga toxin and receptor glycolipid Gb3Cer by surface plasmon resonance. *J Biol Chem*. 276: 42915-42922.

Nutikka A, Lingwood C. 2004. Generation of receptor-active, globotriaosyl ceramide/cholesterol lipid 'rafts' *in vitro*: a new assay to define factors affecting glycosphingolipid receptor activity. *Glycoconj J*. 20:33-38.

Obata F. 2010. Influence of *Escherichia coli* Shiga toxin on the mammalian central nervous system. *Adv Appl Microbiol*. 71:1-19.

Orth-Höller D, Würzner R, 2014. Role of complement in enterohemorrhagic *Escherichia coli*-induced hemolytic uremic syndrome. *Semin Thromb Hemost*. 40:503-507.

Pohlentz G, Steil D, Rubin D, Mellmann A, Karch H, Müthing J. 2019. Pectin-derived neoglycolipids: tools for differentiation of Shiga toxin subtypes and inhibitors of Shiga toxin-mediated cellular injury. *Carbohydr Polym*. 212:323-333.

Raa H, Grimmer S, Schwudke D, Bergan J, Wälchli S, Skotland T, Shevchenko A, Sandvig K. 2009. Glycosphingolipid requirements for endosome-to-Golgi transport of Shiga toxin. *Traffic*. 10:868-882.

Richards A, Kavanagh D. 2009. Pathogenesis and thrombotic microangiopathy: insights from animal models. *Nephron Exp Nephrol*. 113:e97-e103.

Russo D, Parashuraman S, D'Angelo G. 2016. Glycosphingolipid-protein interaction in signal transduction. *Int J Mol Sci*. 17:pii:E1732.

Sandvig K, Bergan J, Dyve AB, Skotland T, Torgersen ML. 2010. Endocytosis and retrograde transport of Shiga toxin. *Toxicon*. 56:1181-1185.

Sandvig K, Bergan J, Kavaliauskiene S, Skotland T. 2014. Lipid requirements for entry of protein toxins into cells. *Prog Lipid Res*. 54:1-13.

Scheutz F, Teel LD, Beutin L, Piérard D, Buvens G, Karch H, Mellmann A, Caprioli A, Tozzoli R, Morabito S, et al. 2012. Multicenter evaluation of a sequence-based protocol for subtyping Shiga toxins and standardizing Stxs nomenclature. *J Clin Microbiol*. 50: 2951-2963.

Schüller S. 2011. Shiga toxin interaction with human intestinal epithelium. *Toxins* (Basel). 3:626-639.

Schütte OM, Patalag LJ, Weber LM, Ries A, Römer W, Werz DB, Steinem C. 2015. 2-Hydroxy fatty acid enantiomers of Gb_3 impact Shiga toxin binding and membrane organization. *Biophys J*. 108:2775-2778.

Sharon N. 2006. Carbohydrates as future anti-adhesion drugs for infectious diseases. *Biochim Biophys Acta*. 1760:527-537.

Smith DC, Lord JM, Roberts LM, Johannes L. 2004. Glycosphingolipids as toxin receptors. *Semin Cell Dev Biol*. 15:397-408.

Smith DC, Sillence DJ, Falguières T, Jarvis RM, Johannes L, Lord JM, Platt FM, Roberts LM. 2006. The association of Shiga-like toxin with detergent-resistant membranes is modulated by glucosylceramide and is an essential requirement in the endoplasmic reticulum for a cytotoxic effect. *Mol Biol Cell*. 17:1375-1387.

Soltyk AM, MacKenzie CR, Wolski VM, Hirama T, Kitov PI, Bundle DR, Brunton JL. 2002. A mutational analysis of the globotriaosylceramide-binding sites of verotoxin VT1. *J Biol Chem*. 277 :5351-5359.

Sonnino S, Prinetti A. 2010. Lipids and membrane lateral organization. *Front Physiol*. 1:153.

Spinale JM, Ruebner RL, Copelovitch L, Kaplan BS. 2013. Long-term outcomes of Shiga toxin hemolytic uremic syndrome. *Pediatr Nephrol*. 28 :2097-2105.

Steil D, Schepers CL, Pohlentz G, Legros N, Runde J, Humpf HU, Karch H, Müthing J. 2015. Shiga toxin glycosphingolipid receptors of Vero-B4 kidney epithelial cells and their membrane microdomain lipid environment. *J Lipid Res*. 56:2322-2336.

Steil D, Pohlentz G, Legros N, Mormann M, Mellmann A, Karch H, Müthing J. 2018. Combining mass spectrometry, surface acoustic wave interaction analysis, and cell viability assays for characterization of Shiga toxin subtypes of pathogenic *Escherichia coli* bacteria. *Anal Chem*. 90:8989-8997.

Stricklett PK, Hughes AK, Ergonul Z, Kohan DE. 2002. Molecular basis for up-regulation by inflammatory cytokines of Shiga toxin 1 cytotoxicity and globotriaosylceramide expression. *J Infect Dis*. 186:976-982.

Te Loo DM, Monnens LA, van der Velden TJ, Vermeer MA, Preyers F, Demacker PN, van den Heuvel LP, van Hinsbergh VW. 2000. Binding and transfer of verocytotoxin by polymorphonuclear leukocytes in hemolytic uremic syndrome. *Blood*. 95:3396-3402.

Trachtman H, Austin C, Lewinski M, Stahl RA. 2012. Renal and neurological involvement in typical Shiga toxin-associated HUS. *Nat Rev Nephrol*. 8:658-669.

Würzner R, Riedl M, Rosales A, Orth-Höller D. 2014. Treatment of enterohemorrhagic *Escherichia coli*-induced hemolytic uremic syndrome (eHUS). *Semin Thromb Hemost*. 40:508-516.

Zhang T, de Waard AA, Wuhrer M, Spaapen RM. 2019. The role of glycosphingolipids in immune cell functions. *Front Immunol*. 10:90.

Zhang W, Mellmann A, Sonntag AK, Wieler L, Bielaszewska M, Tschäpe H, Karch K, Friedrich AW. 2007. Structural and functional differences between disease-associated genes of enterohemorrhagic *Escherichia coli* O111. *Int J Med Microbiol.* 297:17-26.

Zoja C, Buelli S, Morigi M. 2010. Shiga toxin-associated hemolytic uremic syndrome: pathophysiology of endothelial dysfunction. *Pediatr Nephrol*. 25:2231-2240.

Zuverink M, Barbieri JT. 2018. Protein toxins that utilize gangliosides as host receptors. *Prog Mol Biol Transl Sci*. 156:325-354.

Table I. Calculated association k_{ass} and dissociation k_{diss} rate constants and equilibrium dissociation constant K_D for Stx2a and Stx2e using DRMs derived from pHBMECs[a]

Sensor channel	k_{ass} [nM^{-1} s^{-1}][b] Stx2a / Stx2e	k_{diss} [s^{-1}][b] Stx2a / Stx2e	K_D [nM][b] Stx2a / Stx2e
1	1×10^{-4} / n.e.[c]	8×10^{-3} / n.e.[c]	60 / n.e.[c]
2	1×10^{-4} / 7×10^{-5}	8×10^{-3} / 9×10^{-3}	62 / 131
3	1×10^{-4} / 5×10^{-5}	8×10^{-3} / 8×10^{-3}	77 / 178
4	9×10^{-5} / 5×10^{-5}	7×10^{-3} / 7×10^{-3}	85 / 162
5	7×10^{-5} / 4×10^{-5}	7×10^{-3} / 7×10^{-3}	101 / 189
Mean value	1×10^{-4} / 5×10^{-5}	7×10^{-3} / 8×10^{-3}	77 / 165
SD[d]	3×10^{-5} / 1×10^{-5}	6×10^{-4} / 7×10^{-4}	15 / 22

[a]Constants were determined by real-time interaction analysis of Stx2a and Stx2e with sensor surface-coated pooled DRM fractions F1-F3; [b]k_{ass}, k_{diss} and K_D values were obtained for Stx2a (replicate 1) and Stx2e (replicate 2) and correspond to sensorgrams of Figure 6 and Figure 7, respectively; [c]not evaluated due to a technical defect; [d]SD, standard deviation.

Fig. 1. Detection of Stx receptors Gb3Cer and Gb4Cer and the *lipid raft* marker cholesterol in sucrose density gradient fractions of pHBMECs (replicate 1). (**A**) TLC immunochemical detection of Gb3Cer with anti-Gb3Cer antibody and (**B**) Gb4Cer with anti-Gb4Cer antibody; (**C**) manganese chloride-stained cholesterol bands. The membrane preparations applied to detection of Gb3Cer (**A**), Gb4Cer (**B**), and cholesterol (**C**) correspond to 1 x 10^7 cells, respectively. Reference neutral GSLs from human erythrocytes (R) were 10 µg for the anti-Gb3Cer (**A**) and 1 µg for the anti-Gb4Cer overlay assay (**B**). The cholesterol reference R corresponds to 1 µg (**C**). Percentages may not add up to 100.0% due to rounding. The cholesterol percentages with an accuracy of one digital place and the absolute cholesterol amounts in the sucrose density gradient fractions are listed in the Supplementary data, Table SI.

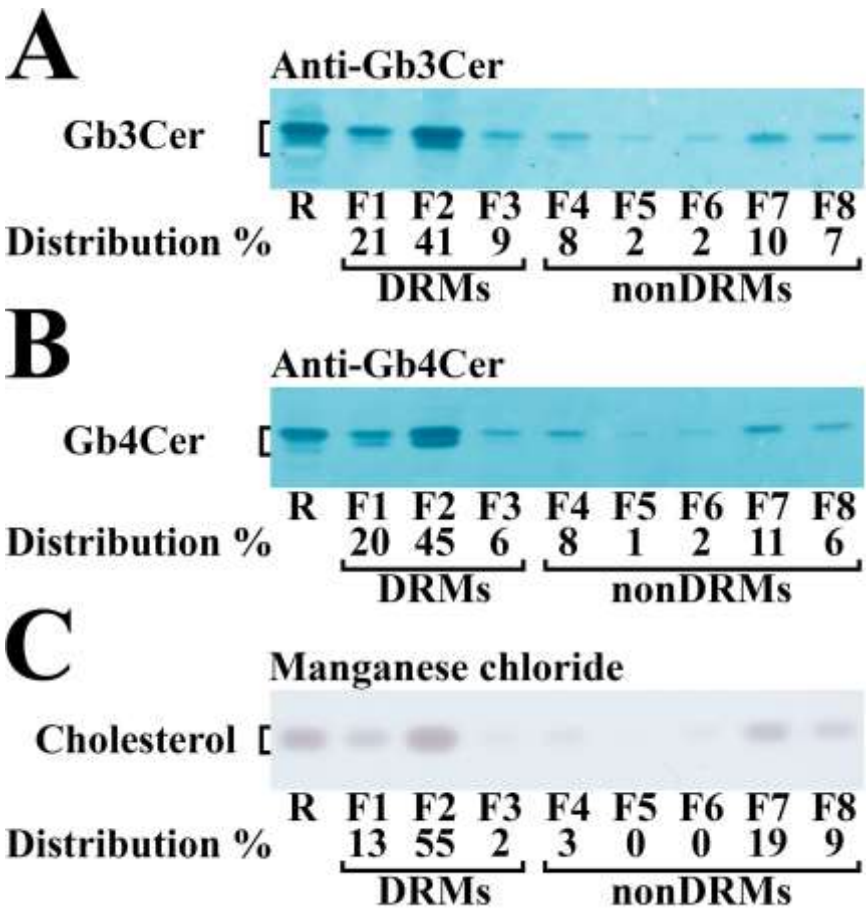

Fig. 2. MS^1 spectra of Gb3Cer (**A**), Gb4Cer (**B**), and PLs (**C**) obtained from DRM fraction F2 of pHBMECs (replicate 1). (**A** and **B**) The GSLs were recorded as monosodiated $[M+Na]^+$ ions in the positive ion mode. Detected structures correspond to Gb3Cer and Gb4Cer lipoforms, carrying uniformly sphingosine (d18:1) and variable C16:0, C22:0, C24:1, or C24:0 fatty acid, are assigned in the spectra. For relative content of Gb3Cer and Gb4Cer in the gradient fractions refer to Figure 1A and Figure 1B, respectively. (**C**) The PL spectrum was recorded in the positive ion mode and the asterisks indicate protonated $[M+H]^+$ ions, while all unmarked ions represent monosodiated $[M+Na]^+$ ions. Gray boxed SM species represent characteristic markers of the liquid-ordered membrane phase (*lipid rafts*).

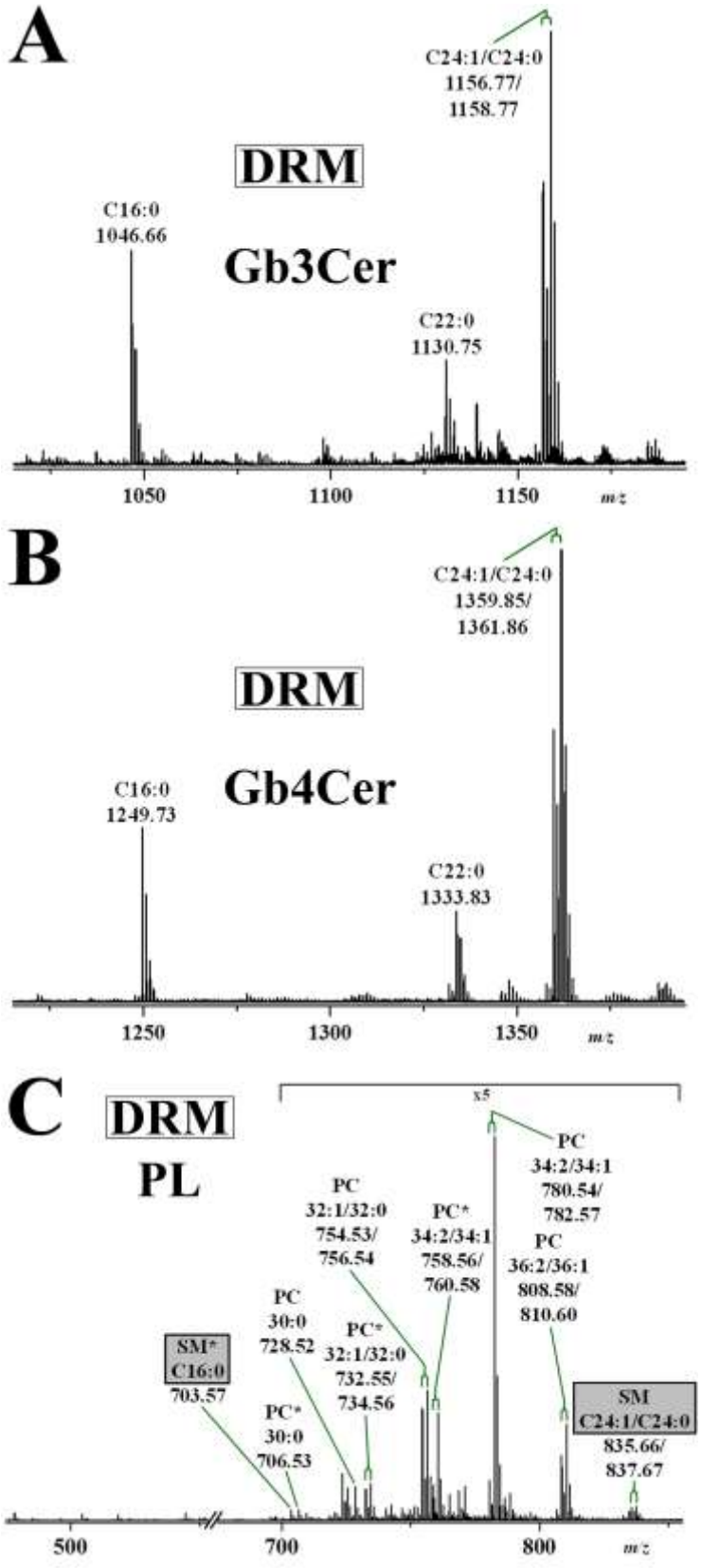

Fig. 3. MS^1 spectra of Gb3Cer (**A**), Gb4Cer (**B**), and PLs (**C**) obtained from nonDRM fraction F7 of pHBMECs (replicate 1). (**A** and **B**) The GSLs were recorded as monosodiated $[M+Na]^+$ ions in the positive ion mode. Detected structures correspond to Gb3Cer and Gb4Cer lipoforms, carrying uniformly sphingosine (d18:1) and variable C24:1 or C24:2 fatty acid, are assigned in the spectra. For relative content of Gb3Cer and Gb4Cer in the gradient fractions refer to Figure 1A and Figure 1B, respectively. The crosses indicate detergent-derived polyethylene glycol oligomers occurring in the nonDRM fractions. (**C**) The PL spectrum was recorded in the positive ion mode and the asterisks indicate protonated $[M+H]^+$ ions, while all unmarked ions represent monosodiated $[M+Na]^+$ ions. Lyso-PC species as markers of the liquid-disordered membrane phase are highlighted as grayed boxes.

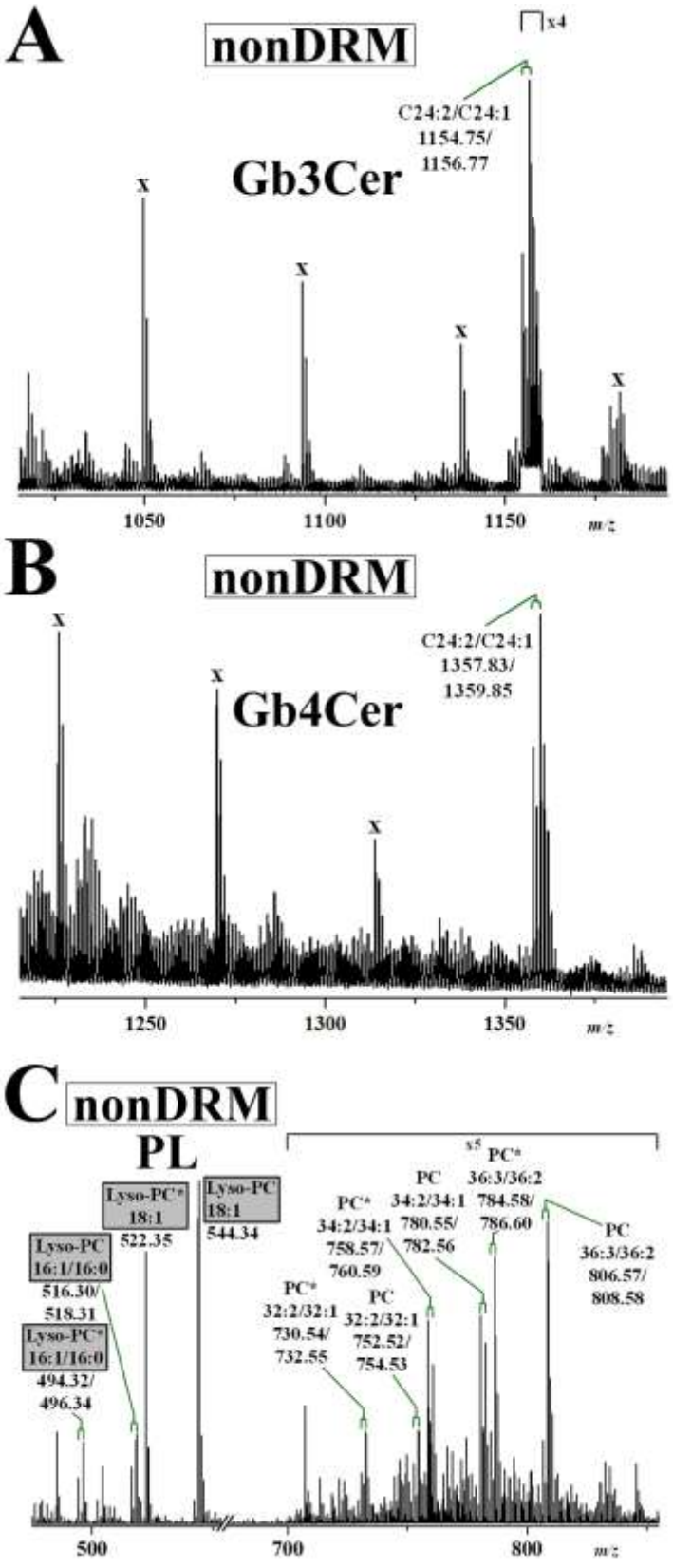

Fig. 4. MS^2 spectrum of Gb3Cer (d18:1, C24:2/C24:1) (**A**) and corresponding fragmentation scheme (**B**) obtained from nonDRM fraction F7 of pHBMECs (replicate 1). The MS^2 spectrum was achieved by CID experiments of the $[M+Na]^+$ precursor ions at *m/z* 1154.75/1156.77 (refer to Figure 3A) and portrays, along with the auxiliary fragmentation scheme, the structural proof of the MS^1-based postulated Gb3Cer lipoform.

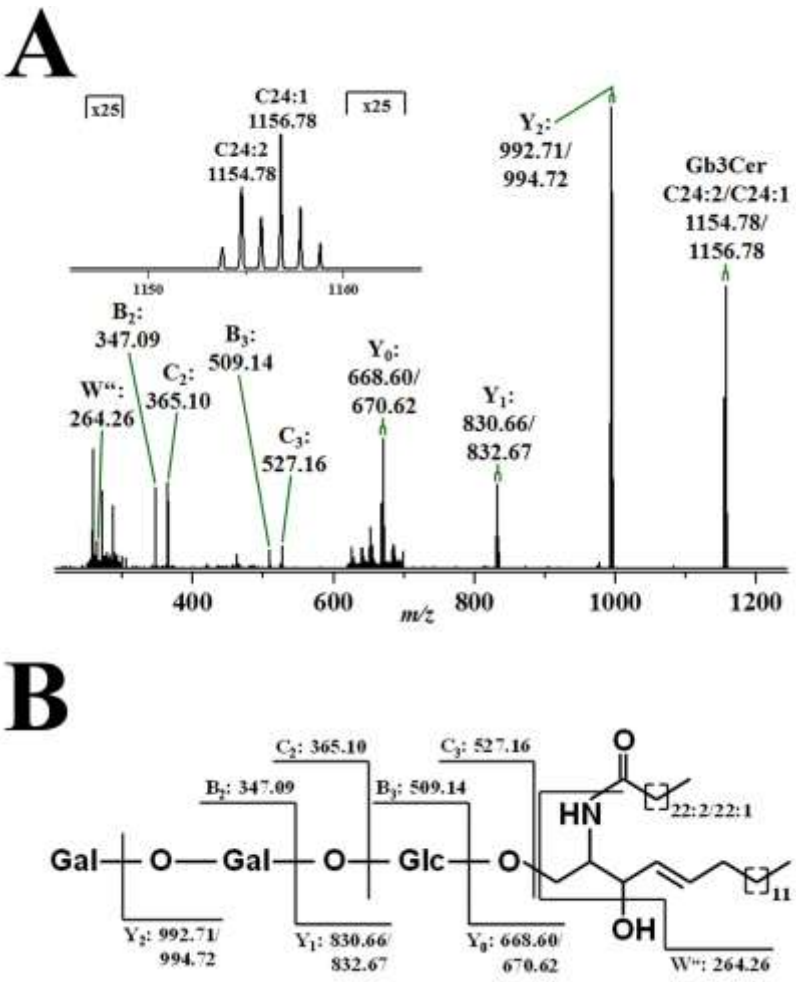

Fig. 5. MS^2 spectrum of Gb4Cer (d18:1, C24:2/C24:1) (**A**) and corresponding fragmentation scheme (**B**) obtained from nonDRM fraction F7 of pHBMECs (replicate 1). The MS^2 spectrum was achieved by CID experiments of the $[M+Na]^+$ predursor ions at *m/z* 1357.83/1359.85 (refer to Figure 3B) and portrays, along with the auxiliary fragmentation scheme, the structural proof of the MS^1-based postulated Gb4Cer lipoform.

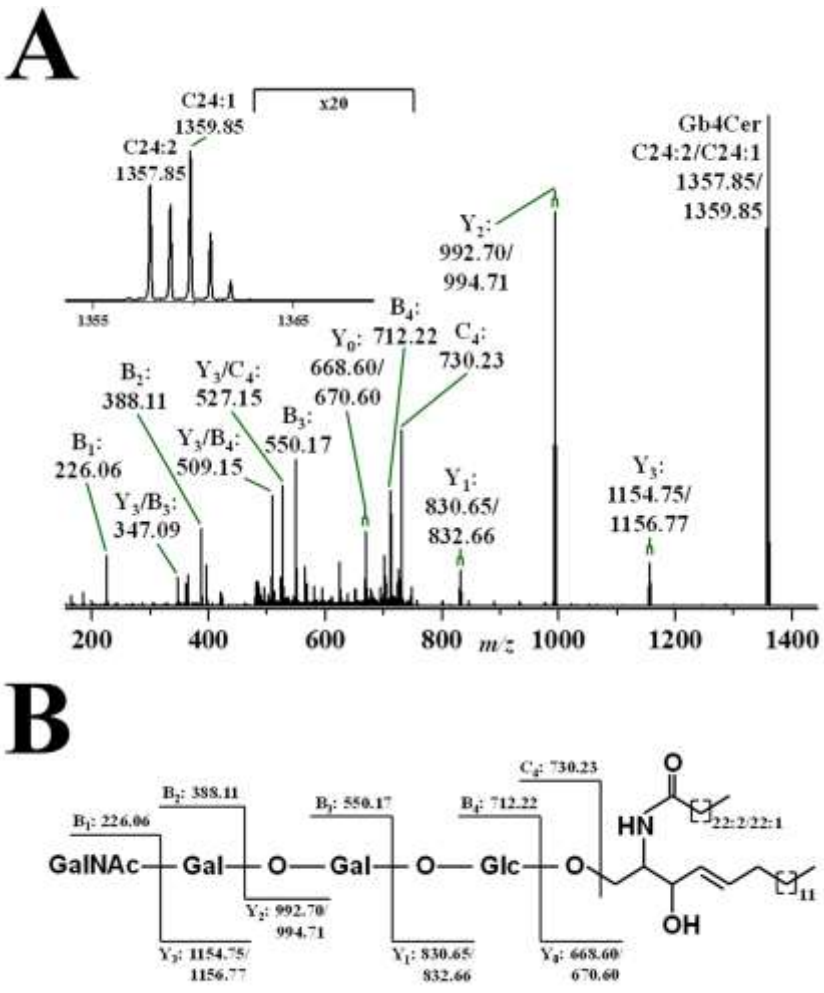

Fig. 6. SAW real-time interaction sensorgrams obtained for binding of Stx2a towards DRM (**A**) and nonDRM fractions (**B**) prepared from pHBMECs (replicate 1). Pooled DRM fractions of F1-F3 (assigned as “DRM” in panel A) and nonDRM fraction F7 (assigned as “nonDRM” in panel B) were employed for biosensor surface coating. (**A**) The binding of Stx2a towards DRM is depicted as association curves (ascending bold lines) and dissociation curves (descending bold lines) using increasing toxin concentrations as indicated. Start: begin of toxin injection; stop: end of toxin injection. The calculated rounded rate constants k_{ass} and k_{diss} and the equilibrium dissociation constant K_D are summarized in Table I. (**B**) The configuration of association and dissociation curves as well as related calculations regarding the interaction of Stx2a towards nonDRM were not feasible due to extremely weak interaction of Stx2a with the nonDRM fraction F7.

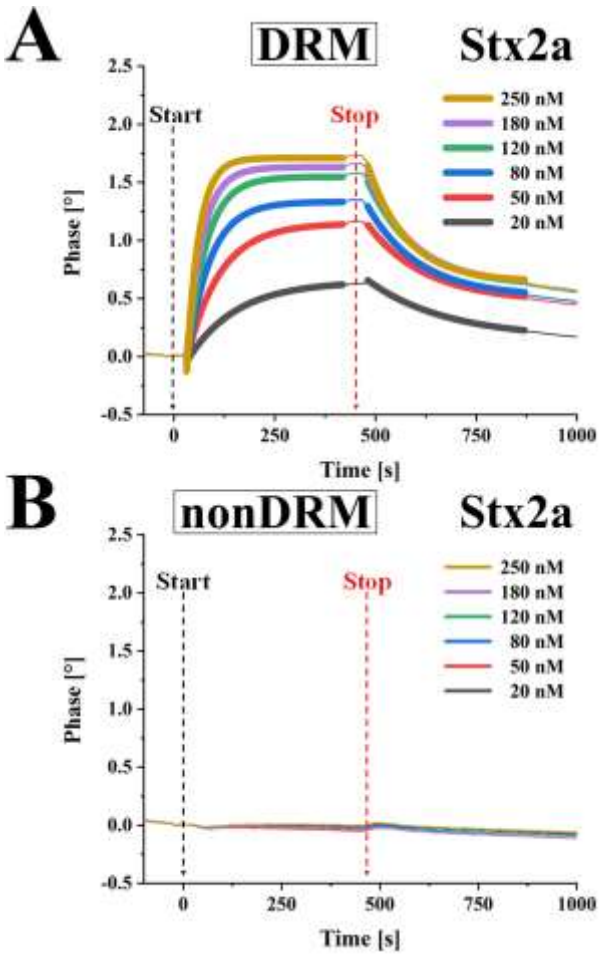

Fig. 7. SAW real-time interaction sensorgrams obtained for binding of Stx2e towards DRM (**A**) and nonDRM fractions (**B**) prepared from pHBMECs (replicate 2). Pooled DRM fractions of F1-F3 (assigned as “DRM” in panel A) and nonDRM fraction F7 (assigned as “nonDRM” in panel B) were employed for biosensor surface coating. (**A**) The binding of Stx2e towards DRM is depicted as association curves (ascending bold lines) and dissociation curves (descending bold lines) using increasing toxin concentrations as indicated. Start: begin of toxin injection; stop: end of toxin injection. The calculated rounded rate constants k_{ass} and k_{diss} and the equilibrium dissociation constant K_D are summarized in Table I. (**B**) The configuration of association and dissociation curves as well as related calculations regarding the interaction of Stx2e towards nonDRM were not feasible due to weak interaction of Stx2e with the nonDRM fraction F7.